

## Three-Dimensional All-Optical Switching Using a Single Diffracting Bessel Beam

Yue Chai<sup>1,2,\*</sup>, Nicolas Marsal,<sup>1,2</sup> and Delphine Wolfersberger<sup>1,2</sup>

<sup>1</sup>Université de Lorraine, CentraleSupélec, LMOPS, Metz F-57000, France

<sup>2</sup>Chair in Photonics, CentraleSupélec, LMOPS, Metz F-57070, France



(Received 17 February 2022; revised 6 May 2022; accepted 12 May 2022; published 30 June 2022)

A single Bessel beam (BB) enables the scalable optical writing of waveguide devices with multiple inputs and outputs in a nonlinear medium. For this purpose, we experimentally propagate a diffracting zero-order BB in a strontium barium niobate photorefractive crystal. Such a configuration can be used for the self-writing of complex waveguiding structures. By tailoring different key parameters such as the diffraction phenomenon through the BB size, the nonlinearity strength through the applied electric field, and the photoinduced refractive-index modulation depth through input beam intensity, our optical platform enables not only the generation of optical splitters but also an all-optical control of the output intensity levels. We also analyze the stability in space and time of the different photoinduced channels. We show that adding a background illumination onto the medium permits a steady-state photoinduced refractive-index modulation with up to nine output channels. These results enrich the research on scalable optical writing techniques for the realization of complex interconnects and enlarge further possibilities for all-optical switching.

DOI: 10.1103/PhysRevApplied.17.064063

### I. INTRODUCTION

In recent years, all-optical switching has drawn much attention in optical communication and computation applications due to its high-speed, reliable, and large-volume data transmission [1]. Several optical switching technologies are based on either mechanical systems such as actuators for moving optical elements or microelectromechanical systems (MEMS) based on neither micromirror arrays nor on optical photoinduced waveguiding structures. Those latter are the most attractive ones because of their low dimension, reconfigurability, scalability, and self-adjusting capabilities even in three dimensions [2]. Creating such optical switchers in the volume of nonlinear materials requires specific direct writing using femtosecond laser pulses [3] or photolithography [4]. Another widespread approach is based on photoinduced waveguides using either Kerr or Pockels effect to artificially design and modulate the refractive-index structure inside a nonlinear material [5,6]. Compared to other methods, photorefractive (PR) materials based on Pockels effect offer the advantages of low input powers (few  $\mu\text{W}$ ) for the photo inscription [7,8]. Indeed, in such materials the free charge carriers are excited by input beams and redistributed through drift and diffusion effects based on the Kukhtarev model equations [9]. The obtained charges' distribution may form a space-charge field creating a refractive-index

modulation through the Pockels effect. The anisotropic behavior of PR materials also plays a role in the situation of two-dimensional (2D) profile beams, which permits stable waveguiding structures to be induced even in two dimensions [10,11]. Gaussian beams were first and most commonly used for photoinducing waveguiding structures [7, 8,10]. More recently, an alternative approach for creating multichannel waveguides uses unconventional beams, for instance Airy beams. Their peculiar features, such as multilobe profile and self-accelerating trajectory, allow inducing addressable waveguides with multiple inputs and outputs for all-optical switching and routing applications [12–17]. Another unconventional beam has been extensively studied due to its nondiffracting characteristics, original self-healing and multilobe profile: the Bessel beam (BB) [18–21]. This beam was proposed by Durnin in 1987 [22] and can be considered as the conical superposition of a set of plane waves. This composition manifests itself by a ring in the Fourier space. By definition, such a beam possesses an infinite energy. To overcome this problem, Durnin proposed to truncate the BB by playing with the aperture of the ring [23]. Another commonly used method based on axicon consists in adding a Gaussian term to generate the so-called Bessel-Gauss beam [24]. Due to this truncation the BB conserves its peculiar features but has a finite diffraction-free distance. Owing to the latest generation of spatial light modulators (SLMs) and the development of optimization algorithms [25], the tailoring of BBs becomes more and more resolved and flexible [26]. Thus, various

\*yue.chai@centralesupelec.fr

studies on BBs have been developed, including the lateral shift during the Mie scattering by a nanosphere [27], the genealogy of leaky modes [28], and the design of controlled switches at millimeter and submillimeter waves for all-optical information processing using BBs [29]. The latter also concerns the application of free-space optical interconnects [30], optical switches in the turbulent atmosphere [31], light localization by inducing Bessel photonic lattices [32], and reconfigurable photoinduced networks [33]. Also in the domain of nonlinear optics, Denz *et al.* realized the induction of various waveguiding configurations in a biased PR material by multiplexing two or four nondiffracting BBs and analyzed their switching characteristics in 2014 [34]. Then in 2018, DelRe *et al.* predicted and experimentally demonstrated the self-trapping and breather-forming behavior of the BB in a PR crystal [35]. Thanks to this phenomenon, Xin *et al.* created multiple waveguides using several diffraction-free BBs in a quadratic nonlinear medium [6] to realize reprogrammable optical components. It is worth noting that all the researches above are based on several nondiffracting BBs interacting under weak nonlinearity. Our recent simulation work in Ref. [36] has numerically demonstrated that complex waveguiding structures with multiple inputs and outputs can be also induced by a single diffracting zero-order BB under high nonlinear conditions.

In this paper, we experimentally demonstrate that only one single diffracting zero-order BB can be used for generating complex three-dimensional waveguiding structures in a bulk photorefractive material [Fig. 1(a)]. By playing with several key parameters such as the BB size, the input beam intensity, the nonlinearity strength, our optical platform offers not only the generation of classical *Y* couplers but also a scenario where nine output channels are localized in both the direction of the ferroelectric *c* axis of the crystal and the perpendicular direction [Fig. 1(b)]. We also study the effect of an external background illumination for stabilizing the corresponding waveguiding structures.

## II. EXPERIMENTAL PLATFORM

Our experiment consists of propagating a single zero-order BB in a PR strontium barium niobate crystal (SBN: Ce) with dimensions  $0.5 \times 0.5 \times 1$  cm ( $n_{\text{SBN}} = 2.3$ ) as depicted in Fig. 1(a). The linear polarized laser beam ( $\lambda = 532$  nm) passing through the half-wave plate (HWP) is expanded by the lenses (L1, L2) then launched onto a SLM where a modulated phase mask similar to an axicon function is applied [37]. Iris 1 enables the selection of the most resolved BB profile among all the diffraction orders produced by the periodic SLM structure. A BB with a few micrometers' size ranging from 6 to  $15 \mu\text{m}$  can be obtained thanks to the inverse telescope made of lenses L3, L4, and Iris 2. Mathematically, the generated zero-order

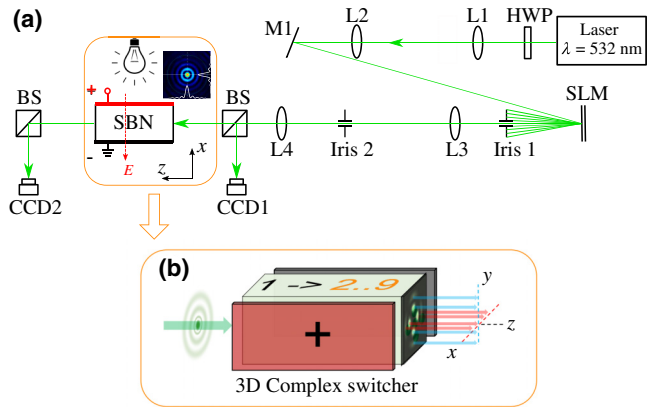


FIG. 1. (a) Experimental setup: HWP, half-wave plate; L, lens; M, mirror; SLM, spatial light modulator; BS, beam splitter. (b) Principle scheme of three-dimensional (3D) complex switcher: single diffracting BB photoinducing nonlinear complex waveguiding structures with multiple possible outputs (from two to nine).

BB is defined as follows:

$$F(r)_{z=0,t=0} = F_0 J_0(k_t \times r) \exp\left(-\frac{r^2}{\omega_0^2}\right), \quad (1)$$

where  $r$  is the transverse coordinate with  $r = \sqrt{x^2 + y^2}$ ,  $J_0$  is the zero-order Bessel function,

$F_0$  is the maximum electric field amplitude of the input BB related to the input beam intensity [ $I_{\text{in}} = |F_0|^2 = P_{\text{in}}/(\pi r_B^2)$ , where  $P_{\text{in}}$  is the input beam power and  $r_B$  is the distance from the beam center ( $x = 0, y = 0$ ) to the furthest point with 13.5% of the maximum intensity],  $k_t$  is the transverse wave number, which is related to the beam size  $r_0$  as  $k_t = 2/r_0$ , and  $\omega_0$  is the waist of the Gaussian truncated term. In all our experiments, we fix  $\omega_0 \approx 90 \mu\text{m}$ , which is enough for inducing a large multilobe structure inside the crystal. The final BB enters the front face of the SBN crystal and propagates along  $L_z$ , the 1 cm length along the  $z$  direction [Fig. 1(a)] of the medium. An external electric field is applied along the crystallographic *c* axis of the crystal corresponding to the polarization direction of the injected BB [( $-x$ ) direction in Fig. 1(a)]. We monitor the input and output profiles of the BB, respectively, at the front and back faces of the SBN crystal by CCD1 and CCD2 cameras.

## III. INFLUENCE OF BB SIZE: FROM SINGLE TO MULTIPLE OUTPUT-CHANNEL ACHIEVEMENTS

It is worth noting that the Gaussian truncated BB defined by Eq. (1) has the diffraction-free distance defined by  $L_D = \omega_0/(k_t/k)$  [24], where  $k$  is the wave number in the SBN crystal. We therefore decide to firstly investigate how

the BB diffraction may affect the waveguiding structures. Figure 2 depicts the output intensity profiles for the non-diffracting and diffracting BBs. Figures 2(a), 2(b), 2(e), and 2(f) represent the output intensity distribution imaged by CCD2 at the exit face of the SBN crystal in the experiments. The white curves are the intensity profiles along, respectively, the  $x$  and  $y$  axis normalized by the maximum value of the linear output intensity. The numbers (1, 2, 3, 4) correspond to the four most intense outputs along  $x$  direction (channel threshold above 20 percent of the total output intensity) and the numbers (1', 2', 3', 4') correspond to the four most intense outputs along  $y$  direction as illustrated in Fig. 2(d) (same for the following figures). Figures 2(c), 2(d), 2(g), and 2(h) show the transverse intensity profiles along the  $c$  axis of the PR crystal ( $x$  direction of the applied electric field) numerically calculated using the (1+1)D model described in Ref. [36] [input profiles (blue lines) and output profiles (red lines)]. In this model, we restrict the BB defined by Eq. (1) in the one-dimensional (1D) situation where the transverse direction corresponds to the  $c$  axis of the PR crystal ( $x$  direction):

$$F(X, Z = 0) = F_0 J_n(X) \exp\left(-\frac{X^2}{(\omega_0 \times k_t)^2}\right), \quad (2)$$

where  $X = k_t x = 2x/x_0$  is the normalized transverse coordinate with  $x_0$  the waist of the main lobe of the zero-order BB, and  $Z = z/L_d$  is the propagating length normalized by  $L_d = kx_0^2/2$ , which is the Rayleigh length of the separated central lobe of the zero-order BB. The nonlinear propagation of this 1D BB can be expressed by

$$i\partial_Z F + \partial_X^2 F = \Gamma E_0 F, \quad (3)$$

In this equation,  $\Gamma = (k^2/k_t^2)n_{\text{SBN}}^2 r_{\text{eff}} E$  represents the nonlinearity strength,  $r_{\text{eff}}$  represents the electro-optical coefficient of the SBN crystal, and  $E$  is the external electric field.  $E_0$  is the space charge field normalized by  $E$ . The temporal evolution of  $E_0$  is calculated by the relaxation-type dynamics equation:

$$\tau \partial_t E_0 + E_0 = -\frac{I}{(1+I)}, \quad (4)$$

where  $\tau = \tau_0/(1+I)$  is the relaxation time of the crystal,  $\tau_0$  is the characteristic response time of the SBN crystal, and  $I = |F|^2$  is the normalized total intensity.

For the experiments, we consider two values of the BB waist: 6  $\mu\text{m}$  ( $k_t = 0.33 \mu\text{m}^{-1}$ ) and 15  $\mu\text{m}$  ( $k_t = 0.13 \mu\text{m}^{-1}$ ). As the diffraction-free distance of the 15- $\mu\text{m}$  BB is much longer than the length of the crystal ( $L_D \approx 1.83 \text{ cm} > L_z = 1 \text{ cm}$ ), the linear output beam has the same transverse profile as the input beam [Fig. 2(a)]. Under strong nonlinear conditions ( $I_{\text{in}} = 0.695 \text{ W/cm}^2$ ,  $E = 3 \text{ kV/cm}$ ), Fig. 2(b) shows that the diffraction-free BB

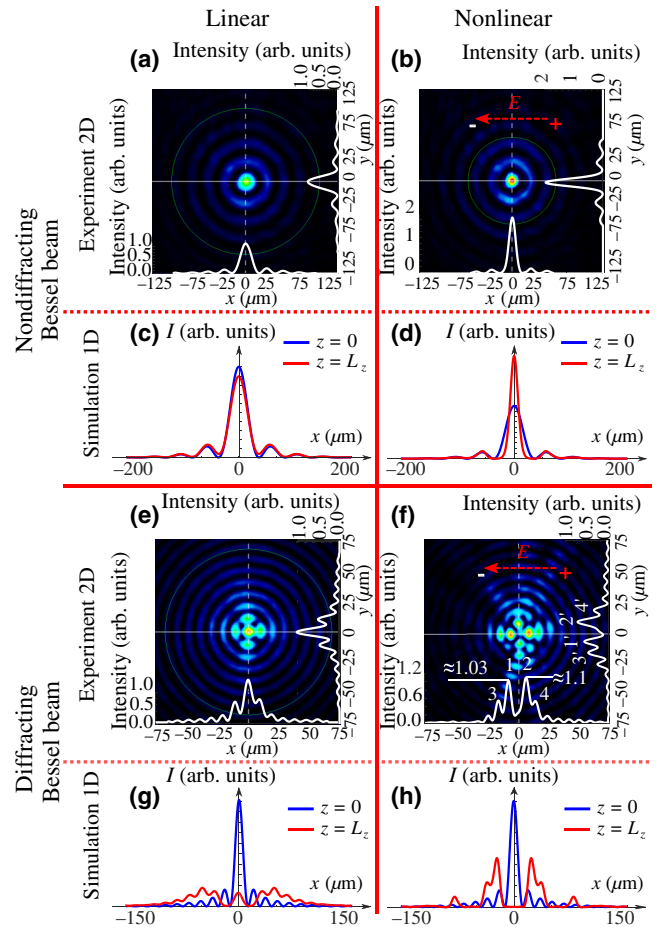


FIG. 2. (a),(b) Diffraction-free configuration: output intensity distribution of the 15- $\mu\text{m}$  zero-order BB propagating in the SBN crystal under (a) linear condition ( $I_{\text{in}} = 0.695 \text{ W/cm}^2$ ,  $E = 0 \text{ kV/cm}$ ) and (b) nonlinear condition ( $I_{\text{in}} = 0.695 \text{ W/cm}^2$ ,  $E = 3 \text{ kV/cm}$ ). (c),(d) Numerical results of the nondiffracting BB calculated using the same model as described in Ref. [36]: the input and output intensity profiles of a 30- $\mu\text{m}$  BB propagating in the SBN crystal under (c) linear condition ( $\Gamma = 0$ ) and (d) nonlinear condition ( $\Gamma = 15$ ). (e),(f) Single diffracting BB configuration: output intensity distribution of the 6- $\mu\text{m}$  zero-order BB propagating in the SBN crystal under (e) linear condition ( $I_{\text{in}} = 124.268 \text{ W/cm}^2$ ,  $E = 0 \text{ kV/cm}$ ) and (f) nonlinear condition ( $I_{\text{in}} = 124.268 \text{ W/cm}^2$ ,  $E = 3.8 \text{ kV/cm}$ ). (g),(h) Numerical transverse profiles of the diffracting BB ( $x_0 = 10 \mu\text{m}$ ) propagating, respectively, under (g) linear ( $\Gamma = 0$ ) and (h) nonlinear condition ( $\Gamma = 3$ ) similar to Figs. 1(b<sub>2</sub>) and 1(c<sub>2</sub>) in Ref. [36]. (Images under nonlinear condition (b),(f) are taken at a transient time catching the maximum output intensity spot.)

has now an intense elliptical focused central spot with a diameter of 9  $\mu\text{m}$  along  $x$  and 10  $\mu\text{m}$  along  $y$  direction, which is a configuration similar to a self-focusing Gaussian beam under nonlinear conditions [38]. These results can be reproduced qualitatively by solving numerically Eqs. (2)–(4). As shown in Fig. 2(c), the input (blue line) and the output (red line) profiles coincide with each other,

which suggests that a nondiffracting BB ( $x_0 = 30 \mu\text{m}$ ) remains constant in its profile when it propagates linearly in the crystal ( $\Gamma = 0$ ). Moreover, under a high nonlinear condition ( $\Gamma = 15$ ), Fig. 2(d) exhibits a narrower and more intense output profile (red line), which is the same as the experimental focusing profile along the  $x$  direction (white line) in Fig. 2(b).

On the other hand, for the 6- $\mu\text{m}$  BB, the diffraction-free distance is now less than the length of the crystal ( $L_D \approx 0.73 \text{ cm} < L_z$ ): the diffraction and consequently the beam distortion cannot be ignored anymore [39]. Thus, as shown in Fig. 2(e), under linear condition ( $E = 0 \text{ kV/cm}$ ) the output beam no longer has a classical multiple-circle profile as the input BB but presents four spots distributed around the central one. When we apply the electric field ( $E = 3.8 \text{ kV/cm}$ ) onto the PR crystal in the ( $-x$ ) direction [as indicated by the red arrow in Fig. 2(f)], the central peak disappears and the optical energy shifts to the adjacent lobes thanks to the drift and the diffusion effects. Indeed, in Fig. 2(f), two well-separated outputs (1, 2) and two other less intense nearby lobes (3, 4) along the  $x$  direction appear. This distribution of energy is consistent with our (1 + 1)D numerical results presented in Ref. [36]. Figures 2(g) and 2(h) are, respectively, similar to figures [Fig. 1(b<sub>2</sub>) and 1(c<sub>2</sub>)] in Ref. [36]. Figure 2(g) shows the diffraction of a small size BB ( $x_0 = 10 \mu\text{m}$ ) propagating linearly ( $\Gamma = 0$ ) in the SBN crystal, and Fig. 2(h) presents that such a BB can induce a waveguiding configuration with four separated lobes under nonlinear conditions ( $\Gamma = 3$ ). The latter [output profile in Fig. 2(h)] presents nearly the same focusing behavior as that shown experimentally along the  $x$  direction in Fig. 2(f), which can be used as a  $Y$  coupler or demultiplexers with four outputs. Overall, the numerical results shown in Figs. 2(c), 2(d), 2(g), and 2(h) are in qualitative good agreement with the  $x$ -direction profiles recorded by the CCD2 [Figs. 2(a), 2(b), 2(e), and 2(f)]. In addition, due to the (2 + 1)D experimental configuration, we also identify four other focusing lobes (1', 2', 3', 4') resulting from the diffusion effect observed along the perpendicular  $y$  direction in Fig. 2(f) giving rise to finally eight channels at the output face of the crystal. We also notice that the intensity distribution is not symmetrically distributed between the  $x$  and  $y$  directions: this is mainly due to the anisotropy of the SBN crystal [40] but this distribution can be adjusted and is developed in the next part of our paper.

#### IV. INFLUENCE OF THE NONLINEARITY: TAILORING THE NUMBER OF OUTPUT CHANNELS

So far, we observe two types of focusing effects depending on the diffraction of the input BB in the biased SBN crystal. The nondiffracting BB ( $r_0 = 15 \mu\text{m}$ ) presents a

self-trapping behavior and induces a solitonlike configuration under nonlinear conditions. In contrast, the 6- $\mu\text{m}$  BB photoinduces multiple output channels unveiling the possibility for creating complex waveguiding structures for all-optical switching. In what follows, we therefore focus our study on this last configuration to see how we can stabilize, balance, and even enlarge the number of outputs.

According to our numerical work in Ref. [36], the nonlinear strength is a key parameter for achieving different waveguiding structures. To specify its impact on the photoinduced configurations, we modify this parameter by increasing the strength of the biased electric field ( $E$ ) and the input BB intensity ( $I_{\text{in}}$ ) in our experiments (Fig. 3). Firstly, we launch the 6- $\mu\text{m}$  zero-order BB with  $I_{\text{in}} = 3.05 \text{ W/cm}^2$  into the front face of the SBN crystal and apply a 1.6 kV/cm electric field in the ( $-x$ ) direction. Figure 3(b<sub>1</sub>) shows the output intensity distributions at the back face of the crystal imaged by CCD2: all results are taken at a transient time catching the maximum output intensity spot but do not concern stationary states that are discussed in the last part of this work. Figures 3(a<sub>1</sub>) and 3(c<sub>1</sub>) show the corresponding profiles along the white lines in Fig. 3(b<sub>1</sub>), respectively, in  $x$  and  $y$  directions. We observe that the output intensity distribution obtained under such a weak nonlinear condition is similar to that obtained under the linear condition [Fig. 2(c)]. Both profiles in  $x$  and  $y$  directions indicate the slight focusing effect on the central peak with a normalized intensity of  $I_{\text{nor}} = 1.06$  and five outputs are potentially addressable. Then we maintain the same input intensity ( $I_{\text{in}} = 3.055 \text{ W/cm}^2$ ) and increase the external electric field to  $E = 2.6 \text{ kV/cm}$  [Figs. 3(a<sub>2</sub>)–3(c<sub>2</sub>)]. Interestingly, the optical energy no longer focuses at the center. The most intense lobe is at position 2 in Fig. 3(a<sub>2</sub>) away from the center in the  $x$  direction and has the normalized intensity of  $I_{\text{nor}} \approx 1.152$ . Moreover, we also notice in Fig. 3(c<sub>2</sub>) two focusing lobes (1', 2') with symmetrical normalized intensities ( $I_{\text{nor}}(1') \approx 0.67$ ,  $I_{\text{nor}}(2') \approx 0.71$ ) and two nearby lobes (3', 4') in the  $y$  direction resulting from the diffusion effect and the anisotropy in this (2 + 1)D configuration. This scenario gives access to nine channels. Furthermore, we increase the input BB intensity to  $I_{\text{in}} = 23.427 \text{ W/cm}^2$  and the external electric field strength up to  $E = 3.8 \text{ kV/cm}$  for achieving a high nonlinear situation. Figure 3(b<sub>3</sub>) shows that the central peak has completely disappeared, and we obtain four outputs (1, 2, 3, 4) [with two well-separated lobes (1, 2)] in the  $x$  direction [Fig. 3(a<sub>3</sub>)] and four outputs (1', 2', 3', 4') [with two well-separated lobes (1', 2')] in the  $y$ -direction [Fig. 3(c<sub>3</sub>)]. In addition, by comparing the profile in Fig. 3(a<sub>2</sub>) with Fig. 3(a<sub>3</sub>) we notice that the normalized intensities of the four lobes (1, 2, 3, 4) all increased. According to the Kukhtarev model [9], light with higher intensity photoexcites more free charge carriers, and a stronger external electric field offers a more intense drift effect. Hence, the focusing phenomenon with

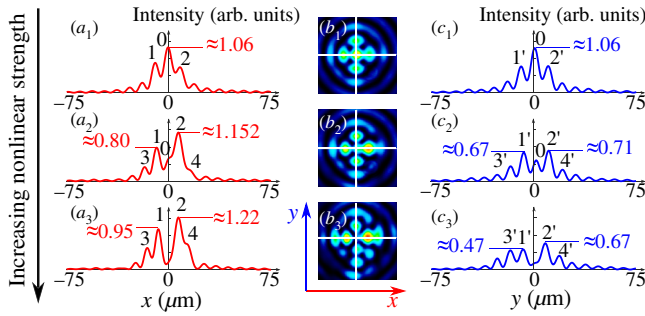


FIG. 3. Configurations induced by the 6- $\mu\text{m}$  zero-order BB propagating in the SBN crystal for increasing nonlinearity. (a<sub>1</sub>), (c<sub>1</sub>) Outputs profiles, respectively, along  $x$  and  $y$  directions under weak nonlinear condition ( $I_{\text{in}} = 3.055 \text{ W/cm}^2$ ,  $E = 1.6 \text{ kV/cm}$ ). (b<sub>1</sub>) 2D intensity distribution corresponding to (a<sub>1</sub>), (c<sub>1</sub>). (a<sub>2</sub>)–(c<sub>2</sub>) Output profiles obtained by increasing the external electric field ( $E = 2.6 \text{ kV/cm}$ ). (a<sub>3</sub>)–(c<sub>3</sub>) Output profiles for increasing both the input BB intensity and the external electric field ( $I_{\text{in}} = 23.427 \text{ W/cm}^2$ ,  $E = 3.8 \text{ kV/cm}$ ).

four lobes, especially along the  $c$  axis ( $x$  direction) of the SBN crystal, becomes more significant as the nonlinearity increases.

In this part, we demonstrate that under high nonlinear conditions, the diffracting zero-order BB can photoinduce multiple 2D output configurations with either five [Figs. 3(a<sub>1</sub>)–3(c<sub>1</sub>)] or nine [Figs. 3(a<sub>2</sub>)–3(c<sub>2</sub>)] and finally eight identifiable outputs [Figs. 2(d) and 3(a<sub>3</sub>)–3(c<sub>3</sub>)]. It is worth noting that all the outputs do not have the same intensity distribution so consequently they have a different refractive-index modulation depth. The guiding efficiency of each channel depends on this modulation depth. Under nonlinear conditions, the latter can be controlled via the power of the input beam and is addressed in the next part of the paper.

## V. INFLUENCE OF THE INPUT BEAM INTENSITY: TAILORING THE GUIDING EFFICIENCY

By comparing the transverse intensity profiles in  $x$  direction of the cases illustrated in Fig. 2(f) (white curve for  $x$  direction) and in Fig. 3(a<sub>3</sub>), respectively, we can notice that intensity amplitudes of lobes (1, 2) are symmetric and nearly similar in Fig. 2(f) but are different (0.95 for lobe 1, 1.22 for lobe 2) in Fig. 3(a<sub>3</sub>). It should be correlated to the input intensity, which is the only different parameter [ $I_{\text{in}} = 124.268 \text{ W/cm}^2$  in Fig. 2(f) and  $I_{\text{in}} = 23.427 \text{ W/cm}^2$  in Figs. 3(a<sub>3</sub>)–3(c<sub>3</sub>)]. Accordingly, we investigate the influence of the input intensity on what is called the refractive-index modulation depth. It could be an interesting way for tailoring the waveguides' guiding efficiency.

We now fix the external biased electric field at  $E = 3.8 \text{ kV/cm}$  and launch the 6- $\mu\text{m}$  zero-order BB into

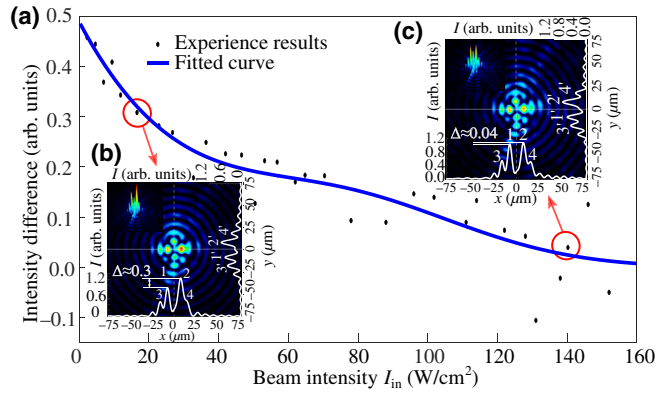


FIG. 4. (a) Difference of the normalized intensities between the outputs (1, 2) versus the input intensity  $I_{\text{in}}$  when the 6- $\mu\text{m}$  zero-order BB propagates in the SBN crystal under a biased 3.8 kV/cm electric field. (b),(c) 2D output intensity distribution induced by the BB for  $I_{\text{in}} = 16.908 \text{ W/cm}^2$  and  $I_{\text{in}} = 142.603 \text{ W/cm}^2$ , respectively.

the SBN crystal with increasingly input intensities. To analyze the fluctuation of the intensity distribution symmetry versus the input intensity, we calculate the values of the normalized intensity difference between the output lobes (1, 2) for each intensity distribution in  $x$  and plot them in Fig. 4(a). The blue line represents the fitted curve corresponding to the experimental data. We present in more details the 2D intensity profile analysis for  $I_{\text{in}} = 16.908 \text{ W/cm}^2$  [Fig. 4(b)] and  $I_{\text{in}} = 142.603 \text{ W/cm}^2$  [Fig. 4(c)], respectively, as examples of the asymmetrical and symmetrical distribution.

As described by the Kukhtarev band transport model [9], photoionized donors are generated in the bright lighted areas. When we apply an electric field in the ( $-x$ ) direction, through the drift effect, the free electron charges are transported to the dark areas in ( $+x$ ) direction and create what is called a space charge field modifying the refractive index through Pockels effect. The area with higher refractive-index variation traps more energy, corresponding to a more intense output spot at the exit face of the crystal. Hence, in the case of light propagation dominated by an electron charge transport and the drift effect, i.e., for an input intensity relatively low (as shown in the example [Fig. 4(b)]), the beam focuses at lobe 2 (in the opposite direction of the electric field) and therefore forms an asymmetric intensity distribution [ $\Delta \approx 0.3$  in Fig. 4(b)]. When we increase the input beam intensity, the diffusion effect becomes stronger and gradually dominates the transport of the charges in the SBN crystal [40]. As a result, the intensity difference between the outputs decreases and tends to  $\Delta = 0$  [ $\Delta \approx 0.04$  as shown in Fig. 4(c)] or even  $\Delta < 0$  (lobe 1 more intense) showing therefore a symmetric output intensity distribution. By the way, we notice that the experimental data fluctuate around the fitted curve for high

input intensity (example  $I_{\text{in}} > 81.487 \text{ W/cm}^2$ ). This instability is due to recording errors related to the short response time of the PR crystal under high input intensity permits the refractive-index modulation depth to be tuned. The two highest-intensity light spot peaks along  $x$  direction tend to be symmetrical as the input intensity rises.

It is worth mentioning that all the above discussions are based on nonlinear light propagation results taken at a transient time catching the maximum output intensity spot but do not concern a stationary state. We will now study and analyse the stability of the waveguides photoinduced by the 6  $\mu\text{m}$  zero-order BB in the biased SBN-crystal.

## VI. INFLUENCE OF A BACKGROUND ILLUMINATION: TAILORING THE WAVEGUIDES' STABILITY

Firstly, we focus on the temporal buildup and behavior of the photoinduced waveguides related to the refractive-index modulation depth. We consider the 6- $\mu\text{m}$  zero-order BB propagation with  $I_{\text{in}} = 23.427 \text{ W/cm}^2$ : in our 1-cm SBN crystal under a biased electric field of  $E = 3.8 \text{ kV/cm}$  [measurement presented in Figs. 3(a<sub>3</sub>)–3(c<sub>3</sub>)]. Figures 5(b<sub>1</sub>)–5(b<sub>5</sub>) show the evolution of the 2D intensity distribution of the output beam versus time. Figures 5(a<sub>1</sub>)–5(a<sub>5</sub>) and 5(c<sub>1</sub>)–5(c<sub>5</sub>) show the corresponding transverse profiles along the red and blue lines in  $x$  and  $y$  direction, respectively, at different moments during the nonlinear focusing process. Starting at time  $t = 0 \text{ ms}$  [Figs. 5(a<sub>1</sub>)–5(c<sub>1</sub>)], the intensity shifts outwards, and forms four well-identifiable lobes in  $x$  direction (1, 2, 3, 4) and four well-identifiable lobes but less intense along  $y$  direction (1', 2', 3', 4') at  $t = 204 \text{ ms}$  as shown in Figs. 5(a<sub>2</sub>) and 5(c<sub>2</sub>). Then, as mentioned in the previous section, the lobes remain in their positions, whereas their intensity peak, especially (1, 2, 1', 2'), gradually increases due to the self-focusing effect. At  $t = 357 \text{ ms}$ , the peak intensity of lobe 2 in Figs. 5(a<sub>3</sub>)–5(c<sub>3</sub>) reaches its maximum in the transient process. Subsequently, the nonlinear phenomenon relaxes and the intensity shifts towards the center [Figs. 5(a<sub>4</sub>)–5(c<sub>4</sub>)] and finally redistributes itself into a Bessel-like profile similar to Figs. 5(a<sub>1</sub>)–5(c<sub>1</sub>) at  $t = 1.6 \text{ s}$  [Figs. 5(a<sub>5</sub>)–5(c<sub>5</sub>)]. It is worth noting that the whole transient process takes less than 2 s. Therefore, it is not possible to induce stationary waveguiding structures that permits a Gaussian probe beam to be guided during several seconds. As shown before, the photorefractive nonlinearity of our system can be tailored by different physical parameters such as the Bessel beam size, the external electric bias field, and the intensity of the input beam  $I_{\text{in}}$ .

In photorefractive systems using Gaussian beams it has also been shown that controlling the so-called dark intensity of the photorefractive crystal  $I_d$  via an external background illumination [Fig. 1(a)] plays a significant role for stabilizing the self-focusing and solitonic regime [41].

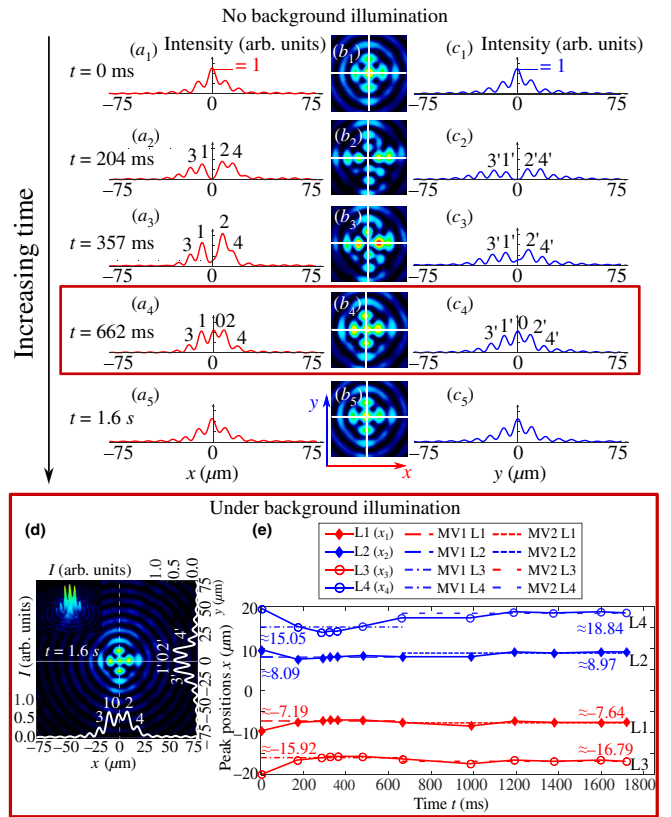


FIG. 5. Nonlinear behavior of the 6- $\mu\text{m}$  zero-order BB propagating in the SBN crystal with parameters ( $I_{\text{in}} = 23.427 \text{ W/cm}^2$ ,  $E = 3.8 \text{ kV/cm}$ ). 1/without any background illumination: (a), (c) temporal evolution of the output profiles along  $x$  and  $y$  directions, respectively, and (b) corresponding 2D intensity distribution at different times: (a<sub>1</sub>)(b<sub>1</sub>)(c<sub>1</sub>)  $t = 0 \text{ ms}$ ; (a<sub>2</sub>)(b<sub>2</sub>)(c<sub>2</sub>)  $t = 204 \text{ ms}$ ; (a<sub>3</sub>)(b<sub>3</sub>)(c<sub>3</sub>)  $t = 357 \text{ ms}$ ; (a<sub>4</sub>)(b<sub>4</sub>)(c<sub>4</sub>)  $t = 662 \text{ ms}$ ; (a<sub>5</sub>)(b<sub>5</sub>)(c<sub>5</sub>)  $t = 1.6 \text{ s}$ . 2/with a background illumination: (d) steady-state 2D intensity distribution for  $t \geq 662 \text{ ms}$ . (e) Output positions of lobes (1, 2, 3, 4) versus  $x$  and  $t$ .

Figure 5(d) in the red frame shows the intensity distribution at  $t = 1.6 \text{ s}$  for  $I_{\text{in}}/I_d = 426$ . We observe five outputs with nearly identical intensity peaks, lobes (0, 1, 2) along  $x$  direction, lobes (0, 1', 2') along  $y$  direction and four outputs nearby, lobes (3, 4) along  $x$  direction, lobes (3', 4') along  $y$  direction. These results are similar to the results presented in Figs. 5(a<sub>4</sub>)–5(c<sub>4</sub>). But the main difference is that, after time  $t = 1.6 \text{ s}$ , the output intensity profile remains constant proving that a steady state is reached. As a result, thanks to the stabilization via the background illumination, we can take advantage of the refractive-index configurations induced by the single diffracting zero-order BB propagating in SBN crystal to guide probe beams. Additionally, the stationary structures induced by such a single beam have nine identifiable outputs, which can be used as waveguides with multiple inputs and outputs. This result provides more opportunities for all-optical switching.

In a second time, we analyze the evolution of the output positions of lobes (1, 2, 3, 4) versus time in the case of  $I_{in} = 23.427 \text{ W/cm}^2$ ,  $E = 3.8 \text{ kV/cm}$  [same as Fig. 5(d)]. We here only consider the output profiles along  $x$  direction (results are similar along the  $y$  direction). Figure 5(e) plots the positions of the lobes [blue lines for lobes (2, 4) in the right and red lines for other lobes (1, 3) in the left] at different increasing times after we apply the external electric field ( $t = 0 \text{ ms}$ ). The corresponding dotted lines present the mean values (MVs) (value indicated next to the lines) of the positions of each lobe versus time. We observe that during a first specific period during  $170 \text{ ms} < t < 662 \text{ ms}$ , the positions of all four outputs (1, 2, 3, 4) remain fixed, which corresponds to the transient self-focusing process with a four-lobe profile as presented in Figs. 5(a<sub>3</sub>)–5(c<sub>3</sub>), without light in the center. After a second time period starting at  $t = 662 \text{ ms}$ , we observe that the 2D intensity distribution relaxes to a less focused state and reaches a steady-state regime [see Fig. 5(d)]: the output lobe positions remain constant and stable over time. As depicted in Ref. [41], the background illumination also influences the self-focusing effect both in the transient and the steady-state regime: for a ratio  $I_{in}/I_d = 426$ , we succeed in stabilizing the photoinduced waveguide structure to the configuration obtained at  $t = 662 \text{ ms}$  [Figs. 5(a<sub>4</sub>)–5(c<sub>4</sub>)] after  $t = 1.6 \text{ s}$ . By changing the intensity ratio, it is therefore possible to stabilize different transient states and following Ref. [41], for a ratio nearly equal to  $I_{in}/I_d = 3$ , the photoinduced waveguide structures can be stabilized in the configuration where the lobe intensities are maximum and well separated [Figs. 5(a<sub>3</sub>)–5(c<sub>3</sub>)]. Unfortunately, regarding the experimental equipment available in our lab, we cannot go under a ratio  $I_{in}/I_d$  of 22.

## VII. CONCLUSION

In conclusion, we experimentally demonstrate that only one single diffracting zero-order BB can be used for generating complex three-dimensional waveguiding structures in a bulk photorefractive material. First, by reducing the BB size under high nonlinear focusing conditions, the influence of the corresponding diffraction has shown that we can tailor the number of output channels (up to eight) whose distributions in terms of intensity and consequently in terms of refractive-index modulation depth are different. Second, we demonstrate that this modulation depth and intrinsically the guiding efficiency of the channels can be finely adjusted by playing with the input intensity of the photoinduced BB giving rise to either symmetrical or asymmetrical waveguiding structures. Third, we study the influence of a background illumination well known in photorefractive systems for stabilizing transient solutions. By adjusting the ratio between the intensity of the BB main lobe and the dark illumination, we prove the stability in terms of time and position of a solution presenting up to

nine potential output channels. Consequently, our optical platform offers not only the possibility to generate classical  $Y$  couplers but also reconfigurable configurations where up to nine output channels are potentially addressable. Our experimental results driven by several easily adjustable key parameters enrich the research on scalable optical writing techniques for the realization of complex interconnects and enlarge further possibilities for all-optical switching. Besides, our experiments are in a two-dimensional situation showing also the results of a weaker focusing effect in the  $y$  direction. As discussed in the Appendix in Ref. [35], due to the diffusion effect and the anisotropic characteristic of the SBN crystal, a weak space-charge field along the  $y$  direction is induced when we apply the external electric field. We also notice that the intensity distributions of the outputs in the  $y$  direction are different with varied parameters such as the nonlinearity strength [Figs. 3(c<sub>2</sub>) and 3(c<sub>3</sub>)]. This phenomenon motivates us to extend our (1 + 1)D numerical model to the (2 + 1)D model for a future work to explore more interesting phenomena in photoinduced waveguiding structures using Bessel beams.

## ACKNOWLEDGMENTS

This work is supported by the Chair in Photonics, Airbus GDI Simulation, Departement de la Moselle, European Regional Development Fund, CentraleSupélec, Fondation Supélec, and Metz Metropole, China Scholarship Council (CSC).

- [1] V. Sasikala and K. Chitra, All optical switching and associated technologies: A review, *J. Opt.* **47**, 307 (2018).
- [2] D. A. Miller, Meshing optics with applications, *Nat. Photonics* **11**, 403 (2017).
- [3] A. Szameit and S. Nolte, Discrete optics in femtosecond-laser-written photonic structures, *J. Phys. B: At., Mol. Opt. Phys.* **43**, 163001 (2010).
- [4] A. C. Urness, E. D. Moore, K. K. Kamysak, M. C. Cole, and R. R. McLeod, Liquid deposition photolithography for submicrometer resolution three-dimensional index structuring with large throughput, *Light: Sci. Appl.* **2**, e56 (2013).
- [5] S. Lan, E. DelRe, Z. Chen, M.-f. Shih, and M. Segev, Directional coupler with soliton-induced waveguides, *Opt. Lett.* **24**, 475 (1999).
- [6] F. Xin, M. Flammini, F. Di Mei, L. Falsi, D. Pierangeli, A. J. Agranat, and E. DelRe, Using Bessel Beams to Induce Optical Waveguides, *Phys. Rev. Appl.* **11**, 024011 (2019).
- [7] S. Lan, M.-f. Shih, and M. Segev, Self-trapping of one-dimensional and two-dimensional optical beams and induced waveguides in photorefractive KNbO<sub>3</sub>, *Opt. Lett.* **22**, 1467 (1997).
- [8] M.-f. Shih, M. Segev, and G. Salamo, Circular waveguides induced by two-dimensional bright steady-state photorefractive spatial screening solitons, *Opt. Lett.* **21**, 931 (1996).

- [9] N. Kukhtarev, V. Markov, S. Odulov, M. Soskin, and V. Vinetskii, in *Landmark Papers On Photorefractive Nonlinear Optics* (World Scientific, 1995), p. 37.
- [10] J. Petter, C. Denz, A. Stepken, and F. Kaiser, Anisotropic waveguides induced by photorefractive (2+1)D solitons, *J. Opt. Soc. Am. B* **19**, 1145 (2002).
- [11] E. DelRe, A. Ciattoni, and A. J. Agranat, Anisotropic charge displacement supporting isolated photorefractive optical needles, *Opt. Lett.* **26**, 908 (2001).
- [12] P. Rose, F. Diebel, M. Boguslawski, and C. Denz, Airy beam induced optical routing, *Appl. Phys. Lett.* **102**, 101101 (2013).
- [13] N. Wiersma, N. Marsal, M. Sciamanna, and D. Wolfersberger, All-optical interconnects using airy beams, *Opt. Lett.* **39**, 5997 (2014).
- [14] N. Wiersma, N. Marsal, M. Sciamanna, and D. Wolfersberger, Airy beam self-focusing in a photorefractive medium, *Sci. Rep.* **6**, 35078 (2016).
- [15] T. Bouchet, N. Marsal, M. Sciamanna, and D. Wolfersberger, Solitonic characteristics of airy beam nonlinear propagation, *Phys. Rev. A* **97**, 051801(R) (2018).
- [16] T. Bouchet, N. Marsal, M. Sciamanna, and D. Wolfersberger, Light-induced interconnects using nonlinear airy beam interactions, *J. Phys. Photonics* **1**, 025001 (2019).
- [17] N. Marsal, N. Wiersma, M. Sciamanna, and D. Wolfersberger, Counterpropagating interactions of self-focusing airy beams, *Sci. Rep.* **9**, 1 (2019).
- [18] J. Arlt, V. Garcés-Chávez, W. Sibbett, and K. Dholakia, Optical micromanipulation using a bessel light beam, *Opt. Commun.* **197**, 239 (2001).
- [19] V. Garcés-Chávez, D. McGloin, H. Melville, W. Sibbett, and K. Dholakia, Simultaneous micromanipulation in multiple planes using a self-reconstructing light beam, *Nature* **419**, 145 (2002).
- [20] D. McGloin and K. Dholakia, Bessel beams: Diffraction in a new light, *Contemp. Phys.* **46**, 15 (2005).
- [21] S. N. Khonina, N. L. Kazanskiy, S. V. Karpeev, and M. A. Butt, Bessel beam: Significance and applications—a progressive review, *Micromachines* **11**, 997 (2020).
- [22] J. Durnin, Exact solutions for nondiffracting beams. I. The scalar theory, *J. Opt. Soc. Am. A* **4**, 651 (1987).
- [23] J. Durnin, J. J. Miceli, and J. H. Eberly, Diffraction-free beams, *Phys. Rev. Lett.* **58**, 1499 (1987).
- [24] F. Gori, G. Guattari, and C. Padovani, Bessel-gauss beams, *Opt. Commun.* **64**, 491 (1987).
- [25] P. A. Sanchez-Serrano, D. Wong-Campos, S. Lopez-Aguayo, and J. C. Gutiérrez-Vega, Engineering of non-diffracting beams with genetic algorithms, *Opt. Lett.* **37**, 5040 (2012).
- [26] A. Vasara, J. Turunen, and A. T. Friberg, Realization of general nondiffracting beams with computer-generated holograms, *JOSA A* **6**, 1748 (1989).
- [27] Z. Cao, W. Liu, Q. Sun, F. Cui, J. Li, F. Xian, S. Pei, and J. Liu, Lateral shifts of linearly-and radially-polarized bessel beams scattered by a nanosphere, *Opt. Express* **30**, 1896 (2022).
- [28] W. Fuscaldo, P. Burghignoli, and A. Galli, Genealogy of leaky, surface, and plasmonic modes in partially open waveguides, *Phys. Rev. Appl.* **17**, 034038 (2022).
- [29] S. C. Pavoneand and W. Fuscaldo, in *2021 15th European Conference on Antennas and Propagation (EuCAP)* (2021), p. 1.
- [30] N. K. Alababneh, Bessel beams and Gaussian beams as information carriers in free space optical interconnects systems: A comparison study, *Int. J. Electr. Comput. Eng.* **9**, 3488 (2019).
- [31] Y. Xie, T. Lei, C. Yang, L. Du, and X. Yuan, Beam waverelieved optical switch using Bessel beams in turbulent atmosphere, *Chin. Opt. Lett.* **17**, 090602 (2019).
- [32] R. Fischer, D. N. Neshev, S. López-Aguayo, A. S. Desyatnikov, A. A. Sukhorukov, W. Krolikowski, and Y. S. Kivshar, Light localization in azimuthally modulated Bessel photonic lattices, *J. Mater. Sci.: Mater. Electron.* **18**, 277 (2007).
- [33] Z. Xu, Y. V. Kartashov, and L. Torner, Reconfigurable soliton networks optically-induced by arrays of nondiffracting Bessel beams, *Opt. Express* **13**, 1774 (2005).
- [34] F. Diebel, D. Leykam, M. Boguslawski, P. Rose, C. Denz, and A. S. Desyatnikov, All-optical switching in optically induced nonlinear waveguide couplers, *Appl. Phys. Lett.* **104**, 261111 (2014).
- [35] M. Flammini, G. Di Domenico, D. Pierangeli, F. Di Mei, A. J. Agranat, and E. DelRe, Observation of Bessel-beam self-trapping, *Phys. Rev. A* **98**, 033808 (2018).
- [36] Y. Chai, N. Bouldja, N. Marsal, and D. Wolfersberger, Multiple input/output waveguides light-induced by a single Bessel beam for all-optical interconnects, *Opt. Express* **29**, 40231 (2021).
- [37] N. Chatrapiban, E. A. Rogers, D. Cofield, W. T. Hill III, and R. Roy, Generation of nondiffracting Bessel beams by use of a spatial light modulator, *Opt. Lett.* **28**, 2183 (2003).
- [38] M. Alonso, C. Dan, D. Wolfersberger, and E. Fazio, Coherent collisions of infrared self-trapped beams in photorefractive InP:Fe, *Appl. Phys. Lett.* **96**, 121111 (2010).
- [39] H. Cheng, C. Xia, S. M. Kuebler, and X. Yu, Aberration correction for SLM-generated Bessel beams propagating through tilted interfaces, *Opt. Commun.* **475**, 126213 (2020).
- [40] J. Petter, C. Weilnau, C. Denz, A. Stepken, and F. Kaiser, Self-bending of photorefractive solitons, *Opt. Commun.* **170**, 291 (1999).
- [41] Z. Chen, M. Segev, and D. N. Christodoulides, Optical spatial solitons: Historical overview and recent advances, *Rep. Prog. Phys.* **75**, 086401 (2012).